RMetS
Royal Meteorological Society

Observation of first and second baroclinic mode Yanai waves in the ocean

Toshiaki Shinoda*†
Naval Research Laboratory, Stennis Space Center, Mississippi, USA

*Correspondence to: T. Shinoda, Naval Research Laboratory, Stennis Space Center, MS 39529, Mississippi, USA.
E-mail: toshiaki.shinoda@nrlssc.navy.mil

The structure and propagation of oceanic Yanai waves (also known as mixed Rossby–gravity waves) are investigated by analysis of satellite-derived sea-surface-height (SSH) data. Significant spectral peaks along the dispersion curves of first and second baroclinic mode Yanai waves are identified by the wavenumber–frequency spectral analysis of SSH for the period 10–17 days. The spatial structure and propagation of these modes are described by an analysis of SSH time series filtered in the frequency–wavenumber domain that includes strong signals along the dispersion curves but excludes those of 17-day tropical instability waves. The difference in meridional structure between the first and second baroclinic modes, which is consistent with theory, is evident. The slow eastward propagation of first and second baroclinic mode Yanai wave packets, which is consistent with the group velocity derived from theory, is also isolated from the SSH data. Year-to-year variability of Yanai wave activity is compared with that of the El Niño–Southern Oscillation (ENSO), showing a moderate correlation with ENSO Modoki. © Published in 2011 by John Wiley & Sons Ltd.

Key Words: Yanai wave; mixed Rossby–gravity wave; equatorial wave; tropical; oceanography; tropical climate variability; ENSO Modoki

Received 17 June 2011; Revised 3 October 2011; Accepted 12 October 2011; Published online in Wiley Online Library

Citation: Shinoda T. 2011. Observation of first and second baroclinic mode Yanai waves in the ocean. *Q. J. R. Meteorol. Soc.* DOI:10.1002/qj.968

1. Introduction

Yanai waves (often referred to as mixed Rossby–gravity waves) play an important role in driving a variety of phenomena in the tropical ocean and atmosphere (e.g. Yanai and Hayashi, 1969; Zangvil, 1975; Liebmann and Hendon, 1990; Takayabu and Nitta, 1993; Lyman *et al.*, 2007). The structure and dispersion relationships of Yanai waves were derived as one of the eigen-modes of the linear shallow-water equation on the equatorial β-plane in the 1960s (Matsuno, 1966). The wave exhibits an eastward group velocity at all wavenumbers. It behaves like a westward propagating Rossby wave in the large negative wavenumber, whereas it has a structure similar to an inertia gravity wave in the large positive wavenumber. Hence, for the negative wavenumber, the wave crest and trough propagate westward whereas the wave energy (packet) propagates eastward with the speed of group velocity. Observational evidence of Yanai waves was presented by the analysis of winds in the lower stratosphere almost at the same time as its theoretical derivation (Yanai and Maruyama, 1966). Since then, many studies discussed its structure, propagation, and generation and forcing mechanisms for both the atmosphere (e.g. Itoh and Ghil, 1988; Hendon and Liebmann, 1991; Takayabu, 1994) and ocean (e.g. Wunsch and Gill, 1976; Moore and Philander, 1977; Weisberg *et al.*, 1979; Zhu *et al.*, 1998).

Using outgoing long-wave radiation (OLR) data, eastward group-propagation of the atmospheric Yanai waves coupled to convection was identified by the combination of wavenumber–frequency spectral analysis and regression analysis (Wheeler and Kiladis, 1999; Wheeler *et al.*, 2000). The period of typical atmospheric Yanai waves is 2–6 days,

and the group velocity is about 5 m s^{-1}, which is shown to be well resolved by the twice-daily OLR data (Wheeler and Kiladis, 1999; Wheeler *et al.*, 2000). Although the period of oceanic Yanai wave is longer (about 10–20 days), the observational evidence of its eastward group-velocity has not been reported because until recently the spatial and temporal resolutions of satellite and *in situ* data were insufficient to explicitly describe the propagation of the wave packet. This situation has begun to change because of the multiple satellite launches in recent years, and the most recent satellite altimetry products are shown to be able to well resolve the signal of oceanic equatorially trapped waves including Yanai waves and to describe their observed dispersion relations (Wakata, 2007; Farrar, 2008, 2011; Shinoda *et al.*, 2009; Shinoda, 2010).

Using the sea-surface-height (SSH) data from recent satellite altimeter measurements, Shinoda (2010) identified prominent spectral peaks along the Yanai wave dispersion curves for the first and second baroclinic modes by wavenumber–frequency spectral analysis. The spatial structure and the phase relationship of 17-day tropical instability waves (TIWs; Lyman *et al.*, 2007) are described by the space and time filtered SSH and sea-surface temperature (SST), showing that the structure of the 17-day TIWs is similar to that of Yanai waves derived from theory. The meridional structure of SSH fluctuation associated with 17-day TIWs is shown to be anti-symmetric with regard to the Equator. The similar anti-symmetric structure is also found in the SST variation associated with 17-day TIWs. However, his analysis did not clearly demonstrate the difference in structure between the first and second baroclinic modes because it focused on showing the structure of TIWs for the period around 17 days, where the spectral peaks along the two dispersion curves are merged in the frequency–wavenumber space.

In this study, we investigate the spectral characteristics, structure and propagation of Yanai waves based on the combination of wavenumber–frequency spectral analysis and cross-correlation (regression) analysis using the most recent version of SSH product from satellite altimeter measurements. The SSH data are filtered in the frequency–wavenumber domain where first and second mode signals are clearly distinguished. Unlike the atmospheric Yanai wave, the signal of the oceanic Yanai wave can be clearly separated into its distinct vertical modes, and thus we are able to describe the spatial distribution and structure of first and second baroclinic mode Yanai waves separately. In addition, the slow eastward propagation of first and second mode Yanai wave packets are isolated, and the propagation speeds of these modes are shown to be consistent with the group velocities obtained from theoretical dispersion curves.

2. Wavenumber–frequency spectral analysis

We use daily multisatellite analysis of SSH anomalies on a $1^\circ \times 1^\circ$ grid over the period 2003–2009. These analyses are obtained from Archiving, Validation and Interpretation of Satellite Oceanographic (AVISO) data. It should be noted that the $1^\circ \times 1^\circ$ gridded daily SSH products are a smoothed version of the measurements, which are derived by objective analysis, and that the actual resolution of the data is still uncertain (e.g. Chelton and Schlax, 2003). Although the daily $1^\circ \times 1^\circ$ SSH products are currently available from October 1992, we use only the recent data from 2003 when measurements from multiple satellites were included in the objective analysis.

Previous studies have demonstrated that the space and time structure of equatorially trapped waves, including Yanai waves, are effectively isolated by the wavenumber–frequency spectral analysis for both the atmosphere and ocean. Here, we first repeat the calculation of wavenumber–frequency spectra performed by Shinoda (2010) using the most recent version of AVISO SSH product. Since the structure of the Yanai wave is anti-symmetric about the Equator, the anomalies of SSH are first decomposed to anti-symmetric and symmetric components (Wheeler and Kiladis, 1999). Then a complex fast Fourier transform (FFT) of SSH anomalies is performed over longitude to decompose SSH into zonal wavenumbers, and an additional FFT is used to determine the spectral power of each resolved wavenumber by frequency. Further details of the analysis are found in Wheeler and Kiladis (1999) and Shinoda *et al.* (2009).

Figure 1 shows contours of the base-10 logarithm of power in wavenumber–frequency space calculated from the anti-symmetric component of SSH anomalies in the equatorial area (5°N–5°S) in the Pacific Ocean (east of 150°E). Solid lines in Figure 1 are the dispersion relationship of Yanai waves for the first and second baroclinic modes:

$$k = \omega/c - \beta/\omega \tag{1}$$

where ω is the angular frequency, k is the wavenumber, c is the internal gravity wave speed, and β is the variation of the Coriolis parameter with latitude. Following Wheeler and Kiladis (1999) and Shinoda *et al.* (2009), the background spectrum is removed from the original spectrum. First, the raw spectra of positive and negative wavenumber domains are averaged to make the spectrum symmetric with regard to wavenumber 0. Then the background spectrum is calculated by applying a 1-2-1 filter multiple times in frequency and wavenumber. Here, the number of passes of the 1-2-1 filter is seven in frequency and four in wavenumber.

Prominent spectral signals of Yanai waves are evident, with their peak corresponding to the dispersion curve of an equivalent depth 0.8 m. This equivalent depth corresponds to equatorial Kelvin waves with a phase speed of ~2.8 m s^{-1}, which is consistent with the first baroclinic mode Kelvin waves in the equatorial Pacific Ocean (e.g. Johnson and McPhaden, 1993; Picaut and Sombardier, 1993; Kessler *et al.*, 1995; Cravatte *et al.*, 2003; Shinoda *et al.*, 2008). Signals of the second baroclinic mode Yanai wave are also found for the equivalent depth of 0.26 m, which is consistent with the second mode Kelvin wave phase speed of ~1.6 m s^{-1} (e.g. Cravatte *et al.*, 2003). The spectral signals of the second baroclinic mode are comparable to those for the first mode.

In order to describe the spatial variation of Yanai wave activity, space and time filtering (via spectral transform) centred around the spectral peak of each mode (the area of the two boxes in Figure 1) is applied to the SSH time series. These areas for the filter are chosen to clearly separate the first and second baroclinic modes. Although significant peaks are found around the period of 17 days because of tropical instability waves (Lyman *et al.*, 2007; Shinoda, 2010), first and second mode dispersion curves are merged around this period. Hence most areas around this period are excluded by the filtering. Note that the time series are not decomposed to symmetric and anti-symmetric components

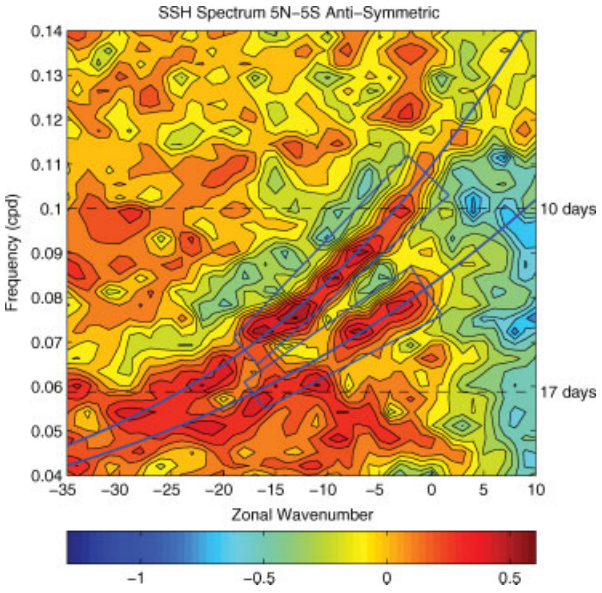

Figure 1. Zonal wavenumber–frequency power spectrum of sea-surface-height anomalies. The colour-bar number indicates the base-10 logarithm. The background power is removed. The curves indicate Yanai wave dispersion relations for equivalent depths of 0.8 m and 0.26 m.

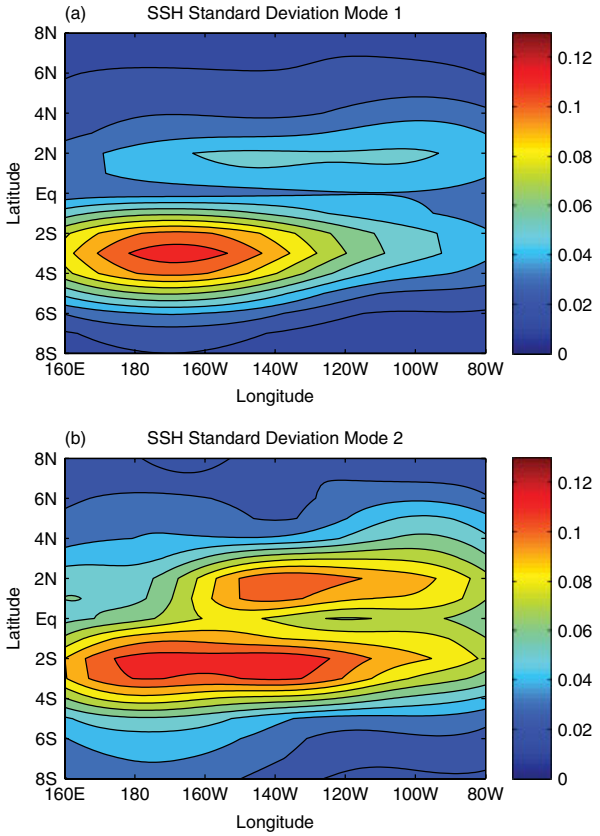

Figure 2. (a) Standard deviation of sea-surface-height anomalies (cm) filtered at periods and wavelengths in the area surrounded by the upper box shown in Figure 1. (b) Same as (a) except for the lower box in Figure 1.

for the filtering. Figure 2(a) shows the standard deviation of SSH time series at each location, which are filtered in space and time for the area surrounded by the upper box in Figure 1. This area covers the significant spectral peak associated with first baroclinic mode Yanai waves. The maximum of SSH fluctuation is found around 3°S, between the dateline and 140°W, and there is another weak local maximum in the Northern Hemisphere around 2°N, between 150°W–120°W.

Figure 2(b) shows the standard deviation of SSH time series for the second baroclinic mode, which are filtered in space and time for the area indicated in the lower box in Figure 1. The spatial pattern of SSH fluctuation is similar but notably different from that for the first baroclinic mode. The

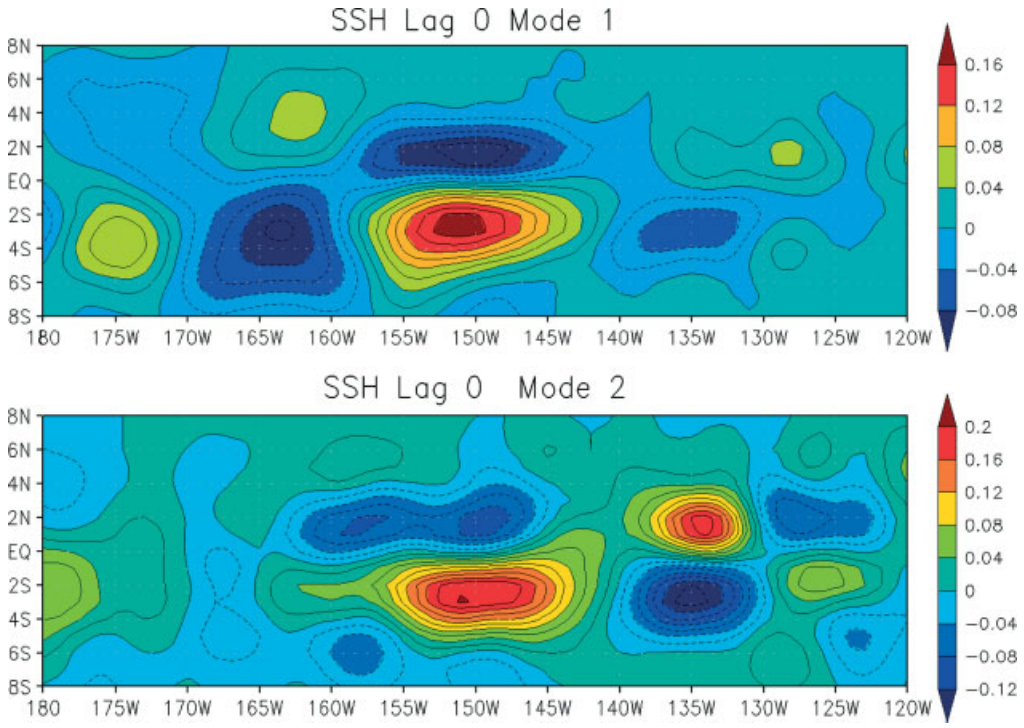

Figure 3. Upper panel: sea-surface-height (SSH) anomalies regressed onto space- and time-filtered SSH anomalies at 2.5°S, 150°W for the first baroclinic mode Yanai wave. Lower panel: same as the upper panel except for the second baroclinic mode.

maximum amplitude is found around 2°S, 180°–120°W. The weaker local maximum in the Northern Hemisphere is also found around 1°N–2°N, between 150°W–120°W.

These spatial distributions of Yanai wave activity are quite different from those associated with 17-day tropical instability waves (TIWs), in which the location of the maximum activity is centred around 120°W in the eastern Pacific (Shinoda, 2010). Because the minimum of mean SST is found on the Equator in the eastern Pacific and thus the sign of meridional SST gradient is opposite in the Northern and Southern Hemispheres, the meridional component of velocity fluctuation associated with Yanai waves generates the SST variation that is anti-symmetric with regard to the Equator. Therefore, significant spectral signals of SST are evident around the 17-day period along the Yanai wave dispersion curves. However, the meridional SST gradient is much weaker in the central Pacific where strong activity of Yanai waves with a 10–16-day period is observed, and thus significant spectral peaks along the Yanai wave dispersion curves for these periods are not found in the SST spectrum (Shinoda, 2010).

The result indicates that the meridional length scale for the first baroclinic mode is larger than that of the second mode, which is at least qualitatively consistent with theory. This difference in meridional structure was not clearly demonstrated for Yanai waves with a 17-day period (Shinoda, 2010). As the two dispersion curves around this period (17 days) are very close in frequency–wavenumber space (see the two boxes of figure 1(b) in Shinoda, 2010), signals of two modes may not be well isolated by the analysis of Shinoda (2010).

The observed meridional structure shows a larger amplitude in the Southern Hemisphere, which is not explained by a linear wave solutions derived from shallow-water equations. The existence of strong mean currents in this region may influence the structure (Lyman *et al.*, 2007). Also, the spatial resolution of the SSH data is not sufficient for further quantitative comparison with theory.

3. Lagged regression analysis

In order to further examine the property of Yanai waves, such as the structure and propagation of individual waves, time series of unfiltered SSH anomalies are regressed against space- and time-filtered SSH anomalies at 2.5°S, 150°W where the large SSH variance is found in both first and second baroclinic modes (Figure 2(a) and (b)). Note that the data are not decomposed to symmetric and anti-symmetric components for the regression analysis. The spatial pattern of SSH fluctuation (Figure 3(a) and (b)) for both first and second baroclinic modes is nearly anti-symmetric with regard to the Equator, which is consistent with the meridional structure derived from theory.

Figure 4 shows the time–longitude (Hovmoller) diagram of the regressed SSH along 3°S for the first and second baroclinic modes. While the westward propagation of individual Yanai waves is evident for both modes, the packet of these waves slowly propagates eastward. The speed of the eastward propagation for the first baroclinic mode is faster than the second baroclinic mode. These signals of slow eastward propagation are consistent with the group velocity of Yanai waves for the first baroclinic mode (1.03 m s^{-1}) and second baroclinic mode (0.64 m s^{-1}) derived from the dispersion curves in Figure 1. Since unfiltered SSH fields are

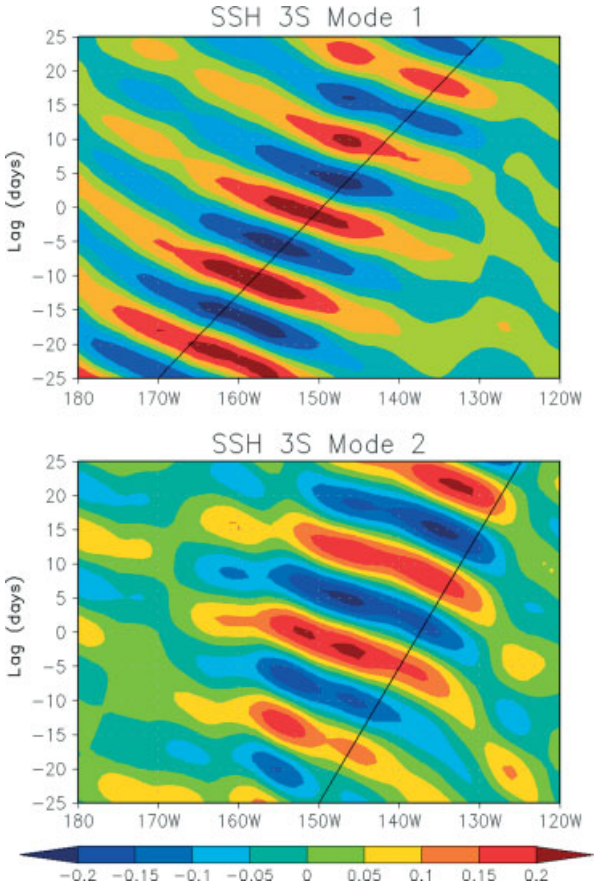

Figure 4. Upper panel: longitude–time diagram of regressed sea-surface-height anomalies for the first baroclinic mode. The solid line indicates the group velocity (1.03 m s^{-1}) for the first baroclinic mode Yanai wave at the wavenumber 4007 km (the global wave number −10 for the horizontal axis in Figure 1) derived from the dispersion curve in Figure 1. Lower panel: same as the upper panel except for the second baroclinic mode of which the group velocity is 0.64 m s^{-1}.

regressed against the Yanai wave filtered time series at the base point, only a real associated signal that is coherent with the base point time series is extracted. Hence, the analysis demonstrates that signals of slow eastward propagation of the Yanai wave packet can be detected from the satellite-derived SSH data.

Longitude–time diagrams of space–time filtered SSH are shown in Figure 5 in order to examine the temporal variation of the Yanai wave amplitude for each vertical mode. While the amplitudes of first and second baroclinic modes are comparable during this period (mid-May 2004 to July 2005), the relative amplitude of each mode depends on the period. The first mode Yanai waves have larger amplitude during June–September 2004, whereas the amplitude of the second mode is larger during January–June 2005. It should be noted that the filtered time series for the same frequency–wavenumber domain display similar eastward propagation of the wave envelope for any field (e.g. red-noise fields) because of the design of the filter, but the temporal variation of wave amplitude for each baroclinic mode can be identified by these filtered time series.

4. Year-to-year variation

Shinoda *et al.* (2009) indicated that the interannual variation of Rossby wave and tropical instability wave activity in the eastern equatorial Pacific is moderately correlated with

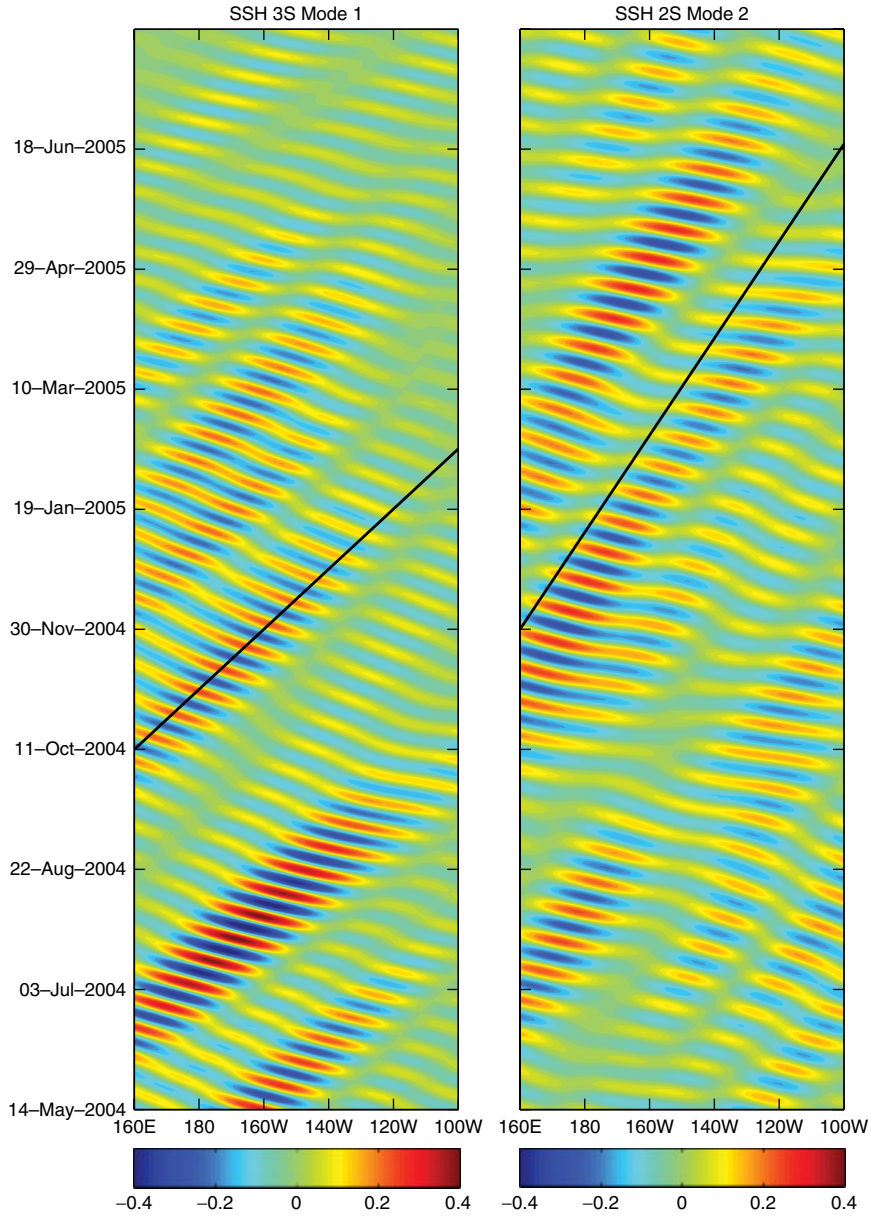

Figure 5. Left panel: longitude–time diagram of sea-surface-height anomalies filtered in the frequency–wavenumber domain indicated in the upper box in Figure 1 for the period 14 May 2004 to 7 August 2005. The solid straight line indicates the group velocity (1.03 m s^{-1}) at the wavenumber 4007 km. Right panel: same as the left panel except that the domain of the filter is indicated in the lower box in Figure 1.

an El Nino–Southern Oscillation (ENSO) index based on the analysis of SSH and SST time series filtered in the frequency–wavenumber domain. Here, the same method as used in Shinoda *et al.* (2009) is applied to investigate the year-to-year variation of Yanai wave activity. The intensity of Yanai wave activity is measured as the standard deviation of the space- and time-filtered SSH time series displayed in Figure 5. Figure 6 shows the monthly time series of first and second baroclinic mode Yanai wave activity for the area 180°–110°W, 4°S–0°, where a significant amplitude of Yanai wave is observed. Time series of first and second modes have some similarities and also notable differences, with a moderate correlation between the two modes (correlation coefficient: $R = 0.54$). For example, activity for both first and second modes is strong during late 2004 and relatively weak during early 2009. Also, a rapid increase of the activity is evident for both first and second modes during 2009. However, the intensity of the second mode is about twice as large as the first mode during most of the periods in 2008. Further quantitative comparisons between first and second modes may not be appropriate since the altimeter product might better resolve the signal of a second mode with a wave period that is longer than the first mode.

The time series of Yanai wave activity are then compared with ENSO indices. Since it has become widely accepted that there are two different types of El Niño in recent years (Larkin and Harrison, 2005; Ashok *et al.*, 2007; Kao and Yu, 2009; Kug *et al.*, 2009), two indices are used for the comparison. These are the Nino3 (150°W–90°W, 5°N–5°S) SST anomaly and the ENSO Modoki Index (EMI; Ashok *et al.*, 2007) defined as

$$\mathrm{EMI} = [\mathrm{SST}]_{\mathrm{A}} - 0.5 \times [\mathrm{SST}]_{\mathrm{B}} - 0.5 \times [\mathrm{SST}]_{\mathrm{C}} \qquad (2)$$

where $[\mathrm{SST}]_{\mathrm{A}}$, $[\mathrm{SST}]_{\mathrm{B}}$ and $[\mathrm{SST}]_{\mathrm{C}}$ are the average SST anomalies over regions A (165°E–140°W, 10°S–10°N), B (110°W–70°W, 15°S–5°N) and C (125°E–145°E, 10°S–20°N) respectively. Monthly SST data from the

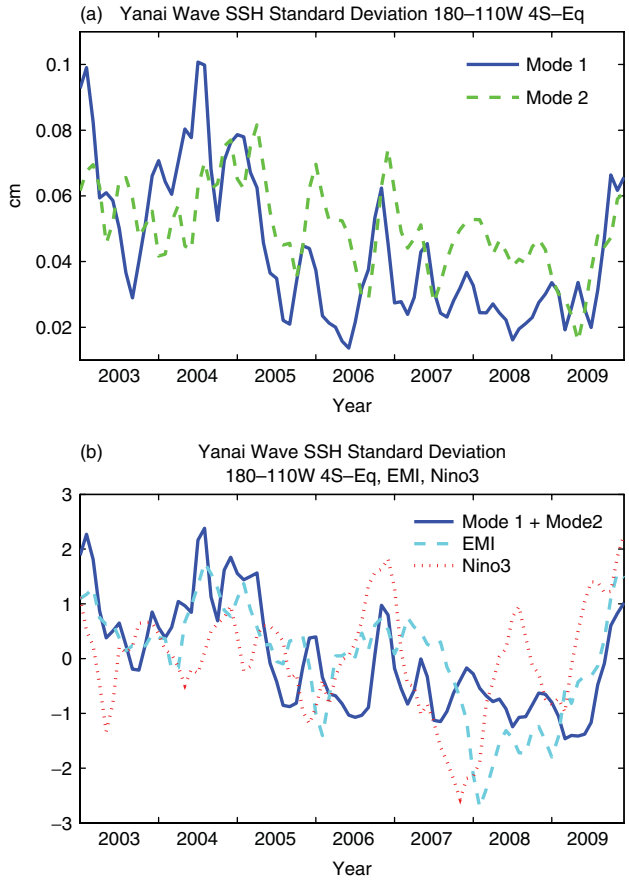

Figure 6. (a) The monthly mean intensity of sea-surface-height (SSH) variability associated with first (solid line) and second (dashed line) baroclinic mode Yanai wave for the area 180°–110°W, 4°S–0°. The intensity is measured by the standard deviation of space- and time-filtered SSH time series. (b) Summation of the two curves in (a) (solid line), ENSO Modoki Index (EMI; dashed line: see text for the detail), and Nino 3 sea-surface temperature anomaly (dotted line). Time series are normalized by their standard deviation and the means are subtracted. This figure is available in colour online at wileyonlinelibrary.com/journal/qj

blended product of satellite/*in situ* observations (Reynolds *et al.*, 2002) are used to calculate EMI and Nino3 SST anomalies. The new type of El Niño is often referred to as El Niño Modoki or Central Pacific El Niño where the maximum SST anomaly is located in the central Pacific, and is flanked by anomalous cold SSTs at the western and eastern ends of the equatorial Pacific.

Figure 6(b) compares the Yanai wave activity with the Nino3 SST anomaly and EMI. While the time series of Yanai wave activity is not similar to the index of the traditional El Nino ($R = 0.25$), it is significantly correlated with EMI ($R = 0.65$). The EMI is better correlated with the first baroclinic mode Yanai wave activity ($R = 0.68$) than the second mode ($R = 0.40$). Whereas the maximum anomalies of SST are located in the eastern Pacific during the traditional El Nino, major SST anomalies during El Nino Modoki events are located in the central Pacific where Yanai wave activity is relatively strong. Hence, large-scale wind anomalies associated with anomalous SSTs in the central Pacific may generate anomalous ocean currents different from those during the traditional El Niño.

A recent study by Shinoda *et al.* (2011) demonstrates that anomalous zonal currents near the Equator show convergence (divergence) with eastward (westward) currents west of the dateline and westward (eastward) currents east of it during the 2004 (2008) El Niño (La Niña) Modoki event. Thus the westward South Equatorial Current (SEC) east of the dateline is enhanced (reduced) during 2004 (2008) El Niño (La Niña) Modoki. The stronger SEC (and thus stronger horizontal shear) during 2004 El Niño Modoki might have an impact upon the subseasonal variance of meridional velocity (and thus generation of Yanai waves) through enhanced instability of equatorial currents. Also, subseasonal (5–20 day period) wind activity is enhanced in the central Pacific east of the dateline during the 2004 El Niño Modoki event in association with the warm SST anomaly (not shown). Subseasonal winds could affect Yanai wave activity through directly generating the meridional component of surface currents. However, the time series discussed here are not long enough to investigate the inter-annual variation associated with ENSO in greater detail. Further observational and modelling studies are necessary to fully understand the physical processes responsible for the significant correlation between Yanai wave activity and the ENSO Modoki.

5. Discussion and conclusions

Unlike the atmospheric equatorial waves, signals of oceanic waves are clearly separated into distinct vertical modes. Therefore the observed structure and group velocity for first and second baroclinic mode oceanic Yanai waves can be compared with theory separately, and the differences between the two modes can be described explicitly. This is not possible for the atmospheric Yanai wave as the distinct equivalent depths of different vertical modes cannot be clearly identified because of the absence of a solid boundary at the top of the troposphere and the interaction between the waves and moist convection. Accordingly, the broad coverage of recent satellite SSH measurements provides excellent data sets to investigate the characteristics of observed equatorially trapped waves such as the phase and group velocities of Yanai waves and their comparison with theory.

Because the time and space resolutions of recent satellite altimetry products are substantially improved, it is now feasible to describe space and time structure of oceanic Yanai waves, including the identification of the spatial distribution of wave activity and the depiction of group velocity. Our statistical analyses clearly demonstrate that signals of Yanai waves can now be detected in daily SSH products derived from the recent satellite measurements. First and second baroclinic mode Yanai waves can be clearly distinguished, and their spatial structure can be isolated. Also, the group velocity for each mode can be explicitly described as a slow eastward propagation of the wave packet. Year-to-year variability of Yanai wave activity is compared with that of the ENSO based on the analysis of space- and time-filtered SSH time series, showing a moderate correlation with the ENSO Modoki. These statistical representations of oceanic Yanai waves are important for understanding their dynamics and generation mechanism, and also useful for evaluating numerical model performances.

Acknowledgements

Valuable discussions with George Kiladis are greatly appreciated. Constructive comments from Dennis Moore and an anonymous reviewer helped improve the original draft of this paper. The altimeter products are produced

by SSALTO/DUACS and are distributed by AVISO. This research is supported in part by the NOAA Modeling, Analysis, Predictions and Projections (MAPP) Program and 6.1 projects including 'The influence of atmosphere–ocean interaction on MJO development and propagation' (Program Elements 601153N) sponsored by the Office of Naval Research.

References

Ashok K, Behera SK, Rao SA, Weng H, Yamagata T. 2007. El Niño Modoki and its possible teleconnection. *J. Geophys. Res.* **112**: C11007, DOI: 10.1029/2006JC003798 268.

Chelton DB, Schlax MG. 2003. The accuracies of smoothed sea surface height fields constructed from tandem altimeter datasets. *J. Atmos. Oceanic Technol.* **20**: 1276–1302.

Cravatte S, Picaut J, Eldin G. 2003. Second and first baroclinic Kelvin modes in the equatorial Pacific at intraseasonal time scales. *J. Geophys. Res.* **108**(C8): 3266, DOI: 10.1029/2002JC001511.

Farrar JT, 2008. Observations of the dispersion characteristics and meridional sea-level structure of equatorial waves in the Pacific Ocean. *J. Phys. Oceanogr.* **38**: 1669–1689.

Farrar JT. 2011. Barotropic Rossby waves radiating from tropical instability waves in the Pacific Ocean. *J. Phys. Oceanogr.* **41**: 1160–1181.

Hendon HH, Liebmann B. 1991. The structure and annual variation of antisymmetric fluctuations of tropical convection and their association with Rossby–gravity waves. *J. Atmos. Sci.* **48**: 2127–2140.

Itoh H, Ghil M. 1988. The generation mechanism of mixed Rossby–gravity waves in the equatorial troposphere. *J. Atmos. Sci.* **45**: 585–604.

Johnson ES, McPhaden MJ. 1993. Structure of interseasonal Kelvin waves in the equatorial Pacific Ocean. *J. Phys. Oceanogr*, **23**: 608–625.

Kao HY, Yu JY. 2009. Contrasting eastern-Pacific and central-Pacific types of ENSO. *J. Climate* **22**: 615–632.

Kessler WS, McPhaden MJ, Weikmann KM. 1995. Forcing of intraseasonal Kelvin waves in the equatorial Pacific. *J. Geophys. Res.* **100**: 10613–10631.

Kug JS, Jin FF, An SI. 2009. Two types of El Niño events: Cold tongue El Niño and warm pool El Niño. *J. Clim.* **22**: 1499–1515, DOI: 10.1175/2008JCLI2624.1.

Larkin NK, Harrison DE 2005. On the definition of El Nino and associated seasonal average U.S. weather anomalies. *Geophys. Res. Lett.* **32**: L13705, 296 DOI: 10.1029/2005GL022738

Liebmann B, Hendon HH. 1990. Synoptic-scale disturbances near the equator. *J. Atmos. Sci.* **47**: 1463–1479.

Lyman JM, Johnson GC, Kessler WS. 2007. Distinct 17- and 33-day tropical instability waves in subsurface observations. *J. Phys. Oceanogr.* **37**: 855–872.

Matsuno T. 1966. Quasi-geostrophic motions in the equatorial area. *J. Meteorol. Soc. Jpn*, **44**: 25–43.

Moore DW, Philander SGH 1977. Modeling of the tropical ocean circulation. In *The Sea*, Vol. 6, Goldberg ED, Cave IN, O'Brien JJ, Steele JH (eds). John Wiley and Sons: New York;. 319–361.

Picaut J, Sombardier L. 1993. Influence of density stratification and bottom depth on vertical mode structure functions in the tropical Pacific. *J. Geophys. Res.* **98**: 18393–18408.

Reynolds RW, Rayner NA, Smith TM, Stokes DC, Wang W. 2002. An improved *in situ* and satellite SST analysis for climate. *J. Climate* **15**: 1609–1625.

Shinoda T. 2010. Observed dispersion relation of Yanai waves and 17-day tropical instability waves in the Pacific Ocean. *Sci. Online Lett. Atmos.* **6**: 17–20, DOI: 10.2151/sola.2010-005.

Shinoda T, Roundy PE, Kiladis GN. 2008. Variability of intraseasonal Kelvin waves in the equatorial Pacific Ocean. *J. Phys. Oceanogr.* **38**: 921–944.

Shinoda T, Kiladis GN, Roundy PE. 2009. Statistical representation of equatorial waves and tropical instability waves in the Pacific Ocean. *Atmos. Res.* **94**: 37–44.

Shinoda T, Hurlburt HE, Metzger EJ. 2011. Anomalous tropical ocean circulation associated with La Nina Modoki. *J. Geophys. Res.Oceans* DOI: 10.1029/2011JC007304.

Takayabu YN. 1994. Large-scale cloud disturbances associated with equatorial waves. Part I: Spectral features of the cloud disturbances. *J. Meteorol. Soc. Jpn* **72**: 433–448.

Takayabu, YN, Nitta T. 1993. 3–5 day period disturbances coupled with convection over the tropical Pacific Ocean. *J. Meteorol. Soc. Jpn* **71**: 221–246.

Wakata, Y. 2007. Frequency–wavenumber spectra of equatorial waves detected from satellite altimeter data. *J. Oceanogr.* **63**: 483–490.

Weisberg, RH, Horigan A, Colin C. 1979. Equatorially trapped Rossby-gravity wave propagation in the Gulf of Guinea. *J. Mar. Res.* **37**: 67–86.

Wheeler M, Kiladis GN. 1999. Convectively coupled equatorial waves: Analysis of clouds and temperature in the wavenumber–frequency domain. *J. Atmos. Sci.* **56**: 374–399.

Wheeler M, Kiladis GN, Webster PJ. 2000. Large-scale dynamical fields associated with convectively-coupled equatorial waves. *J. Atmos. Sci.* **57**: 613–640.

Wunsch C, Gill AE. 1976. Observations of equatorially trapped waves in Pacific sea level variations. *Deep-Sea Res.* **23**: 371–390.

Yanai M, Hayashi Y. 1969. Large-scale equatorial waves penetrating from the upper troposphere into the lower stratosphere. *J. Meteorol. Soc. Jpn* **47**: 167–182.

Yanai M, Maruyama T. 1966. Stratospheric wave disturbances propagating over the equatorial Pacific. *J. Meteorol. Soc. Jpn* **44**: 291–294.

Zangvil A. 1975. Temporal and spatial behavior of large-scale disturbances in tropical cloudiness deduced from satellite brightness data. *Mon. Wea. Rev.* **103**: 904–920.

Zhu XH, Kaneko A, Gohda N, Inaba H, Kutsuwada K, Radenac MH. 1998. Observation of mixed Rossby–gravity waves in the western equatorial Pacific, *J. Oceanogr.* **54**: 133–141.

